

STARFlow: Spatial Temporal Feature Re-embedding with Attentive Learning for Real-world Scene Flow

Zhiyang Lu

Institute of Artificial Intelligence, Xiamen University

zhiyang@stu.xmu.edu.cn

Qinghan Chen

School of Informatics, Xiamen University

kulixiye@gmail.com

Ming Cheng*

School of Informatics, Xiamen University

chm99@xmu.edu.cn

Abstract

Scene flow prediction is a crucial underlying task in understanding dynamic scenes as it offers fundamental motion information. However, contemporary scene flow methods encounter three major challenges. Firstly, flow estimation solely based on local receptive fields lacks long-dependency matching of point pairs. To address this issue, we propose global attentive flow embedding to match all-to-all point pairs in both feature space and Euclidean space, providing global initialization before local refinement. Secondly, there are deformations existing in non-rigid objects after warping, which leads to variations in the spatiotemporal relation between the consecutive frames. For a more precise estimation of residual flow, a spatial temporal feature re-embedding module is devised to acquire the sequence features after deformation. Furthermore, previous methods perform poor generalization due to the significant domain gap between the synthesized and LiDAR-scanned datasets. We leverage novel domain adaptive losses to effectively bridge the gap of motion inference from synthetic to real-world. Experiments demonstrate that our approach achieves state-of-the-art performance across various datasets, with particularly outstanding results on real-world LiDAR-scanned datasets. Our code is available at <https://github.com/O-VIGIA/StarFlow>.

1. Introduction

3D scene flow estimation captures the motion information of objects from two consecutive frames and produces the motion vector for each point in the source frame. It serves as a foundational component for accurately perceiving dynamic environments and provides important motion features to downstream applications, such as object track-

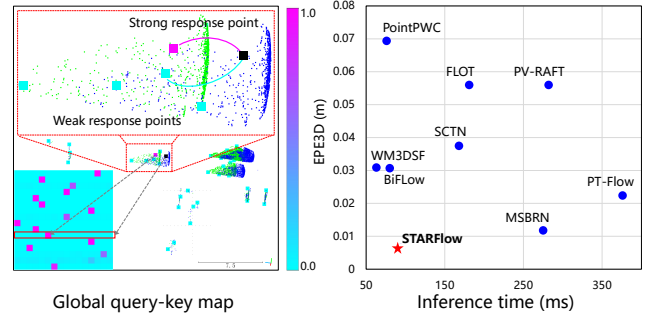


Figure 1. **Left:** Visualization of the global query-key map. Blue and green denote points in the source and target frames respectively. The specific black point is the query point in the source frame, and the heat map of the response key points in the target frame is visualized as the rank of the color bar. The bottom left map denotes the all-to-all query-key heat map for sampled source and target frame points. **Right:** Comparisons of both flow prediction error and inference time on the KITTI dataset. Our model has a real-time inference capability and an acceptable param size (94ms / 9.88M).

ing [35] and human activity estimation [6]. Early approaches rely on stereo or RGB-D images as input. While recent advances in the deep learning-based point cloud processing have paved the way for numerous end-to-end learning-based algorithms specifically designed for scene flow prediction [3, 14, 15, 21, 26, 34]. Among them, FlowNet3D [15] presents a pioneering approach that integrates deep learning into the estimation of scene flow. By incorporating the principles of the PWC (Pyramid, Warp, and Cost volume) optical flow algorithm [24], PointPWC [34] introduces the coarse-to-fine strategy to scene flow prediction. Although previous methods have achieved good results in scene flow tasks, there are still several challenges in this field.

Firstly, the PWC frameworks [3, 4, 14, 27, 28, 34] only account for scene flow regression of the local receptive field

within each level, which neglects global feature matching. Hence, it is difficult to estimate precise motion for long-distance displacements. To this end, a Global Attentive Flow Embedding (GA) module is proposed. Inspired by the global modeling in the transformer [25], we construct a global query-key map (see Figure 1) that considers global matching relations between the source and target frames. This query-key map is then integrated with an all-to-all cost volume based on both feature space and Euclidean space to produce global flow embedding, which is utilized to initialize the scene flow. The second issue is attributed to the warping layer, which upsamples sparse scene flow from the previous level and accumulates to the current level. Previous methods [3, 4, 13, 26, 34] simply employ the information preceding the warping layer to predict the residual flow for the subsequent layer. However, the temporal relation between the consecutive frames changes during warping since the two frames become closer, and the relative spatial position of points within the source frame also transforms due to non-rigid motion. Directly leveraging the previous features could introduce a bias in the prediction. To overcome this limitation, we propose a Spatial Temporal Feature Re-embedding (STR) module to re-embed the temporal features between the warped source frame and target frame, along with spatial features within the warped source frame per se.

Furthermore, as a point-level task, obtaining the ground truth (GT) of scene flow from real-world point clouds is difficult, and previous methods resort to synthetic datasets for training. However, they suffer from domain gaps when applied to real-world LiDAR-scanned scenes. To address this issue, we propose novel Domain Adaptive Losses (DA Losses) based on the intrinsic properties of point cloud motion, including local rigidity of dynamic objects and the cross-frame feature similarity after motion, suggesting promising results when generalized to various real-world datasets.

Overall, our contributions are as follows:

- Our GA module leverages the global attentive mechanism to match the point pairs between two frames globally and constructs the all-to-all cost volume from both 3D Euclidean space and feature space to further obtain the global flow embedding, enabling accurate flow initialization for subsequent residual scene flow prediction.
- We elaborate the STR module to tackle the problems caused by changes in spatiotemporal sequence information of two consecutive frames after warping.
- We propose novel DA Losses that address the synthetic-to-real challenge of scene flow by considering the local rigidity and cross-frame feature similarity.
- Experiments demonstrate that our model achieves state-

of-the-art (SOTA) performance on datasets of various patterns and exhibits strong generalization on real-world LiDAR-scanned datasets.

2. Related Works

FlowNet3D [15] pioneers in leveraging deep learning networks for scene flow based on raw point clouds, which surpasses traditional methods by a large margin. FlowNet3D++ [31] enhances FlowNet3D by incorporating geometric constraints based on point-to-plane distance and angular alignment. FESTA [30] expands on FlowNet3D by utilizing a trainable aggregate pooling to stably down-sample points instead of Farthest Point Sampling (FPS).

Inspired by [24] in optical flow, PointPWC [34] incorporates the Pyramid, Warp, and Cost volume (PWC) to scene flow in a coarse-to-fine manner. Subsequently, numerous approaches persist in employing the PWC-based coarse-to-fine framework for scene flow prediction. HALF [29] introduces a novel double attentive flow embedding in cost volume. RMS-FlowNet [1] integrates random sampling to efficiently process large-scale scenes instead of FPS. Inspired by BERT [5], Bi-PointFlow [3] applies bidirectional flow embedding to produce cost volume using the sequence information. Res3DSF [27] presents a novel context-aware set convolution layer to enhance the detection of recurrent patterns in 3D space. Nonetheless, these coarse-to-fine methods focus on local flow regression layer-by-layer which lacks global information. To address this issue, FlowStep3D [12] aims to directly compute the initial scene flow by leveraging an unlearnable feature similarity matrix. WM3DSF [26] proposes an all-to-all point mixture module with backward reliability validation. However, it is difficult to learn the global matching information of sequences through simple feature concatenation or similarity matrix calculation.

Recently, an increasing number of transformer-based methods have been applied to scene flow estimation. SCTN [13] utilizes sparse convolution for voxel feature extraction and combines it with a transformer-based point feature for accurate scene flow prediction. SAFIT [23] introduces an enhanced transformer to establish object-wise and point-wise relationships, which serves as a feature enhancement module to provide complementary information. PT-Flow [8] is the first integration of the point transformer across the entire scene flow estimation pipeline. RPPformer [14] proposes a point transformer-based pyramidal architecture, which exclusively utilizes relative position-guided point attention layers.

Inspired by transformer [25], we introduce the attention mechanism into the coarse-to-fine approach to globally initialize the scene flow. During local flow refinement, we also design spatiotemporal feature re-embedding on the deformed surfaces of the point clouds after warping.

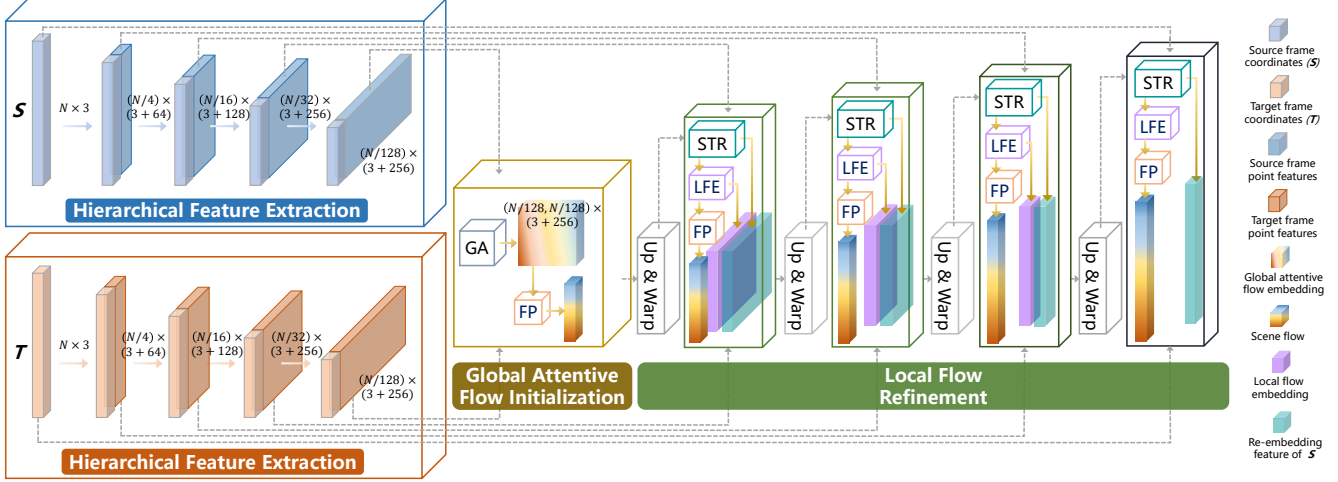


Figure 2. The proposed network. Firstly, semantic features are hierarchically extracted and sent to GA to achieve global matching between the two point clouds at the highest level. Then, the Flow Prediction (FP) module produces the initial scene flow. Subsequently, the flow and features are upsampled level by level, and the upsampled flow is accumulated onto the source frame by the warping layer. Afterwards, Spatial Temporal Feature Re-embedding (STR) and Local Flow Embedding (LFE) are performed in turn, and FP yields the refined flow at a specific level.

3. Methodology

3.1. Problem Definition

The scene flow task aims to estimate point-wise 3D motion information between two consecutive point cloud frames. The input includes the source frame $S = \{s_i\}_{i=1}^N = \{x_i, f_i\}_{i=1}^N$ and target frame $T = \{t_j\}_{j=1}^M = \{y_j, g_j\}_{j=1}^M$, where $x_i, y_j \in \mathbb{R}^3$ are 3D coordinates of the points, and $f_i, g_j \in \mathbb{R}^d$ represent the feature of the corresponding point at a specific level. It should be noted that N and M may not be equal due to the uneven point density and occlusion. The output is the 3D motion vector $SF = \{sf_i \in \mathbb{R}^3\}_{i=1}^N$ of each source frame point, representing the non-rigid motion towards the target frame.

3.2. Hierarchical Feature Extraction

The overview of our proposed network is shown in Figure 2. We utilize PointConv [33] as the feature extraction backbone to build a pyramid network. To extract the higher-level semantic feature S_{l+1} of level $(l+1)$, we apply a three-step process to the previous lower-level feature S_l . FPS is first employed to extract N_{l+1} center points from S_l , where $N_{l+1} < N_l$. Next, K-Nearest Neighbor (KNN) is used to group the neighbor points around each center point. Finally, PointConv is utilized to aggregate the local features for each group, resulting in the desired semantic feature S_{l+1} .

3.3. Global Attentive Flow Embedding

The GA module is designed to capture the global relation between consecutive frames during the flow initialization. After performing the multi-level feature extraction, we obtain

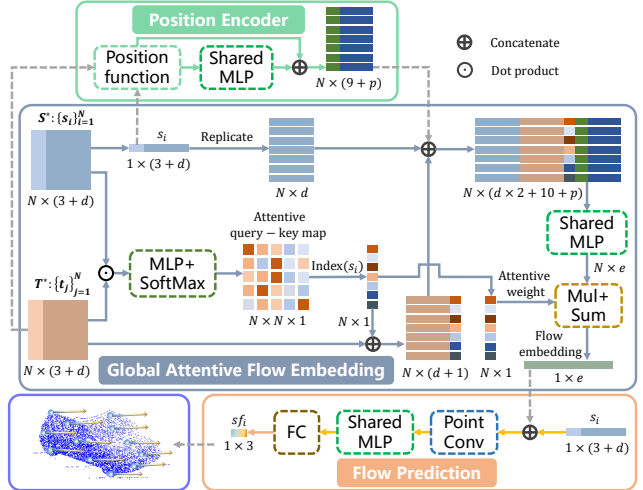


Figure 3. Flowchart of global attentive flow initialization, where the GA module takes the high-dimensional semantic features of point clouds as input and globally embeds point pairs in Euclidean and feature spaces. This embedded feature is then aggregated using the global query-key map to obtain the global attentive flow embedding, based on which the FP module generates the initial scene flow.

S^* and T^* at the highest level of the pyramid. Following that, we construct the global flow embedding from a specific point s_i in S^* to all point t_j in T^* , as shown in Figure 3.

We first compute the similarity correlation between s_i and t_j utilizing dot product \odot . Then a global query-key map $W = \{W_{ij}\}$ is constructed by leveraging the Multi-Layer Perception (MLP) to find the correlation of all point pairs

across frames:

$$W_{ij} = \sigma(\text{MLP}(f_i \odot g_j)), \quad (1)$$

where σ denotes Softmax. Afterward, to establish the relative positional association between point pairs, a position encoder PE^* in Euclidean space is introduced as follows, where η denotes concatenation.

$$PE_{ij} = \eta(x_i, y_j, y_j - x_i), \quad (2)$$

$$PE_{ij}^* = \eta(PE_{ij}, \text{MLP}(PE_{ij})). \quad (3)$$

We proceed to construct the all-to-all cost volume $AC = \{AC_{ij}\}$ from both feature space and Euclidean space. The cost of point pair s_i and t_j is represented as:

$$AC_{ij} = \text{MLP}(\eta(f_i, g_j, W_{ij}, PE_{ij}^*)). \quad (4)$$

Finally, the cost volume is aggregated by utilizing the global query-key map W , to obtain the global attentive flow embedding at the specific point s_i of the source frame:

$$GAFE_i = \sum_j W_{ij} AC_{ij}. \quad (5)$$

Once $GAFE = \{GAFE_i\}$ has been obtained, it is then fed into the flow predictor (described in Section 3.6) to generate the global initial scene flow.

3.4. Warping Layer

We employ distance-inverse interpolation to upsample the coarse sparse scene flow from level $(l + 1)$ to obtain the coarse dense scene flow of level l . The obtained coarse dense flow is directly accumulated onto the source frame S_l to generate the warped source frame $WS_l = \{ws_i\}_{i=1}^{N_l} = \{wx_i = x_i + sf_i, f_i\}_{i=1}^{N_l}$, which brings the source and target frames closer and allows the subsequent layers to only consider the estimation of residual flow [3, 8, 12, 26, 32, 34].

3.5. Spatial Temporal Feature Re-embedding

After the warping layer, the spatiotemporal relation between the consecutive frames may undergo changes. Specifically, the temporal features of points from the warped source frame to the target change since the position between the two point clouds is closer. Furthermore, dynamic non-rigid objects in the source frame may encounter local surface distortion during motion, resulting in different spatial features. Therefore, it is necessary to re-embed spatiotemporal point features in the source frame before the Local Flow Embedding (LFE), which is implemented in a patch-to-patch manner between the two frames following [34]. Based on this consideration, we re-embed the spatiotemporal features of each point ws_i at level l based on the warped source frame WS_l and the target frame T_l , as depicted in Figure 4.

Temporal Feature Re-embedding First, we locate the K nearest neighbor points group $\mathcal{N}_T(ws_i)$ of point ws_i in T_l .

For each target point $t_j \in \mathcal{N}_T(ws_i)$, by employing position encoder as (2), a 9D positional feature PE_{ij} is acquired for this group, representing the positional relation between the two frames after warping. Then, the initial temporal re-embedding feature is derived using the following formula:

$$TRF_{ij} = \text{MLP}(\eta(g_j, f_i, PE_{ij})). \quad (6)$$

Instead of employing the hard aggregation method of Max-pooling, which results in flow bias due to the non-corresponding points between the two frames, we leverage local similarity map $LM_i = \{LM_{ij}\}$ in both feature space and Euclidean space to derive the soft aggregation weights,

$$LM_{ij} = \sigma(\text{MLP}(\eta(TRF_{ij}, \text{MLP}(PE_{ij})))), \quad (7)$$

$$TRF_i^* = \sum_j LM_{ij} TRF_{ij}. \quad (8)$$

Spatial Feature Re-embedding Spatial feature re-embedding shares the same framework as temporal feature re-embedding, with the only distinction being that the embedding object changes to the warped source frame itself.

Upon acquiring the temporal re-embedding features $TRF^* = \{TRF_i^*\}$ and spatial re-embedding features $SRF^* = \{SRF_i^*\}$ of each point in the warped source frame of level l , we fuse them by leveraging the fusion network to derive the ultimate comprehensive features

$$STRF_i = \text{MLP}(\eta(TRF_i^*, SRF_i^*)), \quad (9)$$

and the warped frame updates to $WS_l = \{wx_i, STRF_i\}_{i=1}^{N_l}$. As shown in Figure 2, the STR module is followed by LFE, which computes the patch-to-patch cost volume of each point ws_i by utilizing the spatiotemporal re-embedding features.

3.6. Flow Prediction

This module is constructed by combining PointConv, MLP, and a Fully Connected (FC) layer. For each point s_i in the source frame, its local flow embedding feature, along with the warped coordinates and $STRF_i$ are input into the module. PointConv is first employed to incorporate the local information of each point, followed by non-linear transformation in the MLP layer. The final output is the scene flow sf_i , regressed through the FC layer.

4. Training Losses

4.1. Hierarchical Supervised Loss

A supervised loss is directly hooked to the GT of scene flow, and we leverage multi-level loss functions as supervision to optimize the model across various pyramid levels. The GT of scene flow at level l is represented as $\tilde{SF}_l = \{\tilde{sf}_i^l\}_{i=1}^{N_l}$ and the predicted flow is $SF_l = \{sf_i^l\}_{i=1}^{N_l}$. The multi-level supervised loss is as follows:

$$\mathcal{L}_{sup} = \sum_{l=1}^5 \frac{\delta_l}{N_l} \sum_{i=1}^{N_l} \|\tilde{sf}_i^l - sf_i^l\|_2, \quad (10)$$

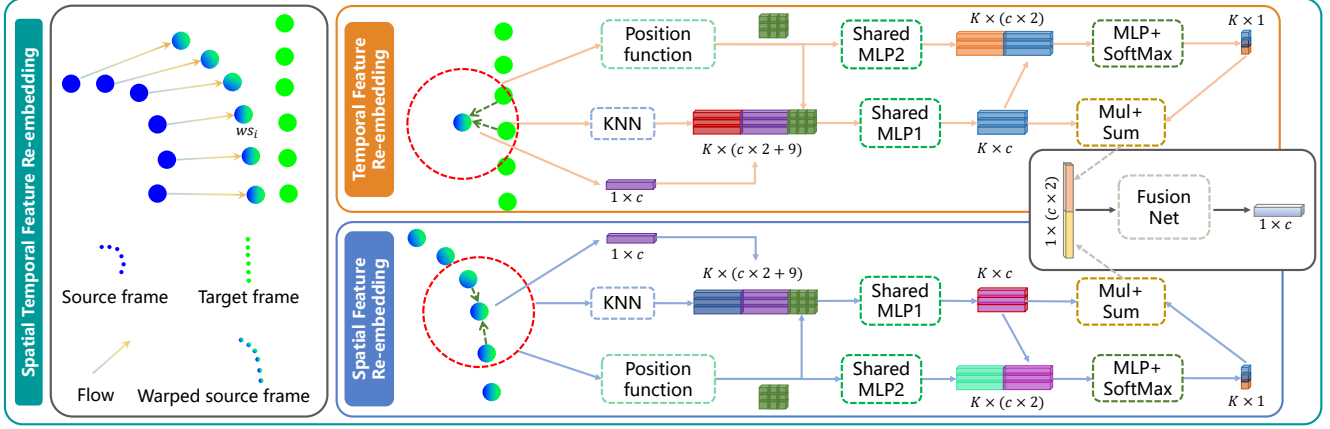


Figure 4. The details of STR module. For a specific warped point ws_i , Spatial Feature Re-embedding (SFR) searches for KNN points of ws_i in the warped source frame and aggregates them by employing local weights learned from both feature space and Euclidean space, while Temporal Feature Re-embedding (TFR) aggregates the KNN points around ws_i within the target frame. The resulting SFR and TFR features are combined and fed into the fusion network to obtain the final aggregated features.

where δ is the penalty weight for each level, with $\delta_1 = 0.02$, $\delta_2 = 0.04$, $\delta_3 = 0.08$, $\delta_4 = 0.16$, and $\delta_5 = 0.32$.

4.2. Domain Adaption Losses

Local Flow Consistency (LFC) Loss Dynamic objects in real-world scenes may not exhibit absolute rigid or regular motion. Instead, they typically undergo local rigid motion, which is manifested through the consistency of local flow. We quantify the degree of predicted flow difference between each point s_i and its KNN+Radius points group $\mathcal{N}_S^R(s_i)$ in the source frame at the full resolution level ($N_1 = 8192$) as the LFC loss, where point $p \in \mathcal{N}_S^R(s_i)$ denotes $p \in \mathcal{N}_S(s_i)$ and the ℓ_2 distance between p and s_i is less than R . The KNN+Radius search strategy effectively mitigates the influence of noise points resulting from occlusion and sparsity in point clouds, as demonstrated in Figure 5. Formally, the LFC loss is represented as follows:

$$\mathcal{L}_{lfc} = \frac{1}{N_1} \sum_{i=1}^{N_1} \frac{1}{|\mathcal{N}_S^R(s_i)|} \sum_{s_j \in \mathcal{N}_S^R(s_i)} \|sf_i - sf_j\|_2, \quad (11)$$

where $|\cdot|$ is the number of points in a group.

Cross-frame Feature Similarity (CFS) Loss The semantic features of the points in the warped source frame are similar to those in the surrounding target frame, as their point cloud data should be in a dynamic registered state. Specifically, we accumulate the GT scene flow \tilde{sf} directly onto the source frame at the full resolution level, as described by $\tilde{ws}_i = \{x_i + \tilde{sf}_i, STRF_i\}$. Next, we utilize cosine similarity to compute the similarity between \tilde{ws}_i and $t_j \in \mathcal{N}_T^R(\tilde{ws}_i)$ in the target frame:

$$CS(\tilde{ws}_i, t_j) = \frac{STRF_i \odot g_j}{\|STRF_i\|_2 \|g_j\|_2}. \quad (12)$$

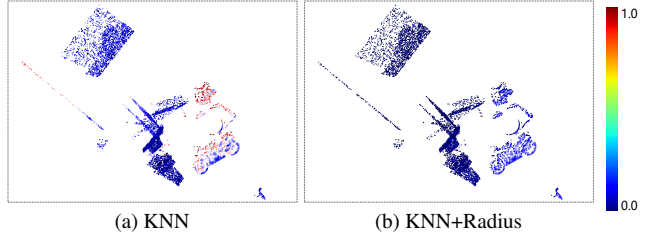


Figure 5. The differences of ground truth scene flow local consistency under different nearest point search methods. The normalized value is shown in the right color bar.

It is noteworthy that owing to the non-rigid deformation that transpires during motion, the initial features of points within the source frame and the target frame may not be similar. However, through continual warping and spatiotemporal feature re-embedding, the corresponding points between the two frames gradually reach a high local feature similarity effect. For this reason, we utilize the features of source frame points derived from the last layer of the STR module (the rightmost re-embedding feature shown in Figure 2) as input instead of the initially extracted features. Lastly, we establish a similarity threshold TH and employ function F to penalize points that exhibit a similarity lower than TH :

$$\mathcal{L}_{cfs} = \frac{1}{N_1} \sum_{i=1}^{N_1} \sum_{t_j \in \mathcal{N}_T^R(\tilde{ws}_i)} \frac{F(CS(\tilde{ws}_i, t_j) - TH)}{|\mathcal{N}_T^R(\tilde{ws}_i)|}, \quad (13)$$

where $F(x) = -x$ if $x < 0$ and 0 otherwise, and g_j is obtained by triple interpolations of the semantic features of the next-level sparse point clouds.

The final loss of our model is :

$$\mathcal{L}_{all} = \lambda_1 \mathcal{L}_{sup} + \lambda_2 \mathcal{L}_{lfc} + \lambda_3 \mathcal{L}_{cfs}, \quad (14)$$

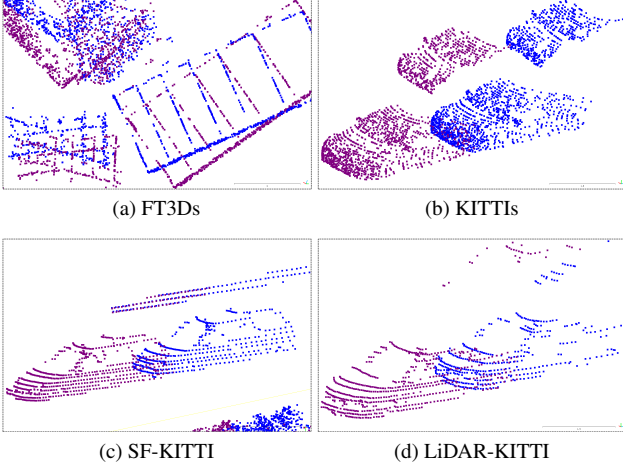


Figure 6. Comparisons of datasets with various patterns, including (a) synthetic stereo, (b) real-world stereo, and (c)(d) real-world LiDAR-scanned. Blue and purple denote the source and target frames, respectively.

where $R = 0.05$, $TH = 0.95$, and $\lambda_1 = 0.7$, $\lambda_2 = 0.15$, $\lambda_3 = 0.15$ by default.

5. Experiments

5.1. Datasets and Data Preprocessing

The experiments were performed on four datasets: the synthetic dataset FlyThings3D (FT3D) [17] and three real-world datasets including Stereo-KITTI [18, 19], SF-KITTI [7], and LiDAR-KITTI [9, 10].

FT3D is a synthetic dataset generated from ShapeNet [2], where random motions are assigned to each object within every scene, and Stereo-KITTI is a real-world dataset. These datasets are preprocessed in two ways [11, 15]: FT3Ds and KITTI remove non-corresponding points between consecutive frames, while FT3Do and KITTIo retain occluded points using mask labels.

FT3D and Stereo-KITTI datasets are derived from dense and regular disparity images, distinct from real-world LiDAR-scanned datasets, as shown in Figure 6. To showcase the robustness of our STARFlow, we also conducted experiments on real-world LiDAR-scanned datasets SF-KITTI and LiDAR-KITTI, which emphasize sparse and non-corresponding point attributes. Following [7], the SF-KITTI dataset is only used for training. Further dataset details can be found in the supplementary material.

5.2. Experimental Settings

Implementation Details The architecture of our model comprises a total of 5 levels. We take $N_1 = M_1 = 8192$ points as input, randomly sampled from source and target frames if they contain different numbers of points. Within the multi-layer pyramid network, the down-sampled points

vary across different levels, with $N_2 = 2048$, $N_3 = 512$, $N_4 = 256$, and $N_5 = 64$, respectively. Notably, the 5th layer is referred to as the GA module. Our model is implemented with PyTorch 1.9, and both training and testing are conducted on a single NVIDIA RTX3090 GPU. The AdamW optimizer [16] with $\beta_1 = 0.9$ and $\beta_2 = 0.99$ is used for model tuning during the training phase, with an initial learning rate of 0.001 which was decayed by half every 80 epochs. We train our model in an end-to-end manner for 900 epochs (or reached convergence) with batch size 8. Our model code and weights are both available.

Evaluation Metrics Following previous methods [3, 7, 10, 21, 26, 34], we employ the same evaluation metrics for fair comparisons, including EPE3D (m), Acc3D Strict, Acc3D Relax, Outliers3D, EPE2D (px), and Acc2D, which are discussed in detail in our supplementary material.

5.3. Results

Our method exhibits remarkable generalization ability across various scenarios, encompassing both synthetic and real-world scenes, as well as dense or sparse point clouds. In contrast, some previous methods are tailored to specific datasets.

FT3Ds and KITTI We compare with recent SOTA methods on the FT3Ds dataset. Additionally, we evaluate the generalization of STARFlow by directly testing it on the KITTI dataset without any fine-tuning. The quantitative results presented in Table 1 clearly indicate that STARFlow outperforms the other methods. Specifically, on the FT3Ds dataset, STARFlow is on par with SOTA [4] while achieving a 66% reduction in inference time. Further, our model exhibits exceptional generalization performance on the KITTI dataset, surpassing the second place by 46% on EPE3D. Qualitative analysis is shown in Figure 7.

FT3Do and KITTIo Similar to the above, we train our model on FT3Do and test on KITTIo without any fine-tuning. The experimental results are listed in Table 2, which reveal the good performance of our model even with occlusion. Specifically, our model achieves 39% improvement over the previous SOTA method [4] on FT3Do. Furthermore, STARFlow outperforms [4] by a significant margin, surpassing it by 33% and 40% in terms of EPE3D and Outliers on the real-world occluded KITTIo dataset, respectively. Visualized experimental results are provided in the Figure 8.

Generalization on LiDAR-KITTI To validate the generalization on real-world LiDAR-scanned datasets, we train our model on FT3Ds and SF-KITTI datasets separately, followed by evaluation on the LiDAR-KITTI dataset. The results are shown in Table 3 and the right part of Figure 8. Specifically, STARFlow reduces EPE3D by 50% and 16% compared to the FH-Net [7] under training on FT3Ds and SF-KITTI datasets, respectively, which proves that our model also has strong motion inference ability even on the sparse

Dataset	Method	Sup.	EPE3D (m)↓	Acc Strict↑	Acc Relax↑	Outliers↓	EPE2D (px)↓	Acc2D↑
FT3Ds	SPFlowNet [22]	Self	0.0606	0.6834	0.9074	0.3876	–	–
	PointPWC [34]	Full	0.0588	0.7379	0.9276	0.3424	3.2390	0.7994
	PV-RAFT [32]*	Full	0.0461	0.8169	0.9574	0.2924	–	–
	SCTN [13]	Full	0.0383	0.8474	0.9681	0.2686	–	–
	Bi-PointFlow [3]	Full	0.0282	0.9184	0.9781	0.1436	1.5822	0.9296
	WM3DSFNet [26]	Full	0.0281	0.9290	0.9817	0.1458	1.5229	0.9279
	MSBRN [4]*	Full	0.0158	0.9733	0.9923	0.0568	0.8335	0.9703
	STARFlow (Ours)	Full	0.0143	0.9767	0.9942	0.0615	0.7831	0.9742
KITTI	SPFlowNet [22]	Self	0.0362	0.8724	0.9579	0.1771	–	–
	PointPWC [34]	Full	0.0694	0.7281	0.8884	0.2648	3.0062	0.7673
	PV-RAFT [32]	Full	0.0560	0.8226	0.9372	0.2163	–	–
	Bi-PointFlow [3]	Full	0.0307	0.9202	0.9603	0.1414	1.0562	0.9493
	WM3DSFNet [26]	Full	0.0309	0.9047	0.9580	0.1612	1.1285	0.9451
	PT-Flow [14]*	Full	0.0224	0.9551	0.9838	0.1186	0.9893	0.9667
	MSBRN [4]*	Full	0.0118	0.9713	0.9893	0.0856	0.4435	0.9853
	STARFlow (Ours)	Full	0.0064	0.9961	0.9993	0.0792	0.3189	0.9983

Table 1. Performance comparisons on the FT3Ds and KITTI datasets. All models in the table are only trained on FT3Ds and no fine-tuning is applied when tested on KITTI. The best results for each dataset are marked in bold. * denotes the methods with an inference time exceeding 250 ms.

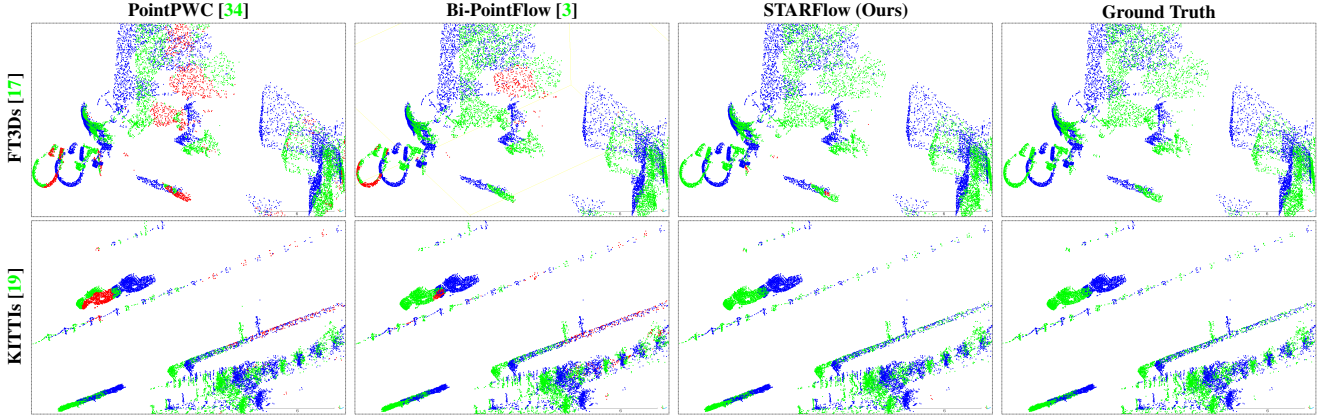


Figure 7. The visualization comparisons among PointPWC, Bi-PointFlow, and our method by training conducted only on FT3Ds. The blue represents the source frame, and the green represents the result of warping the source frame using predictions. The red signifies incorrectly predicted warped points whose EPE3D > 0.1m.

Dataset	Method	EPE3D (m)↓	Acc Strict↑	Acc Relax↑	Outliers↓
FT3Do	OGSF [20]	0.1217	0.5518	0.7767	0.5180
	Bi-PointFlow [3]	0.0730	0.7910	0.8960	0.2740
	WM3DSF [26]	0.0630	0.7911	0.9090	0.2790
	MSBRN [4]	0.0535	0.8364	0.9261	0.2314
	STARFlow (Ours)	0.0326	0.9152	0.9742	0.1398
KITTIo	OGSF [20]	0.0751	0.7060	0.8693	0.3277
	Bi-PointFlow [3]	0.0650	0.7690	0.9060	0.2640
	WM3DSF [26]	0.0730	0.8190	0.8900	0.2610
	MSBRN [4]	0.0448	0.8732	0.9500	0.2085
	STARFlow (Ours)	0.0298	0.9606	0.9740	0.1237

Table 2. Comparisons on the FT3Do and KITTIo datasets. All methods are trained only on FT3Do.

Method	Training set	EPE3D (m)↓	Acc Strict↑	Acc Relax↑	Outliers↓
FlowNet3D [15]	FT3Ds	0.722	0.030	0.122	0.965
PointPWC [34]	FT3Ds	0.390	0.387	0.550	0.653
FLOT [21]	FT3Ds	0.653	0.155	0.313	0.837
Rigid3DSF [10]	FT3Ds	0.535	0.262	0.437	0.742
FH-L [7]	FT3Ds	0.531	0.200	0.397	0.825
STARFlow (Ours)	FT3Ds	0.265	0.438	0.620	0.599
FlowNet3D [15]	SF-KITTI	0.289	0.107	0.334	0.749
PointPWC [34]	SF-KITTI	0.275	0.151	0.405	0.737
FLOT [21]	SF-KITTI	0.271	0.133	0.424	0.725
FH-L [7]	SF-KITTI	0.255	0.241	0.538	0.683
FH-R [7]	SF-KITTI	0.156	0.341	0.636	0.612
STARFlow (Ours)	SF-KITTI	0.131	0.516	0.849	0.429

Table 3. Evaluation results on LiDAR-KITTI.

and indirect corresponding LiDAR-scanned point clouds.

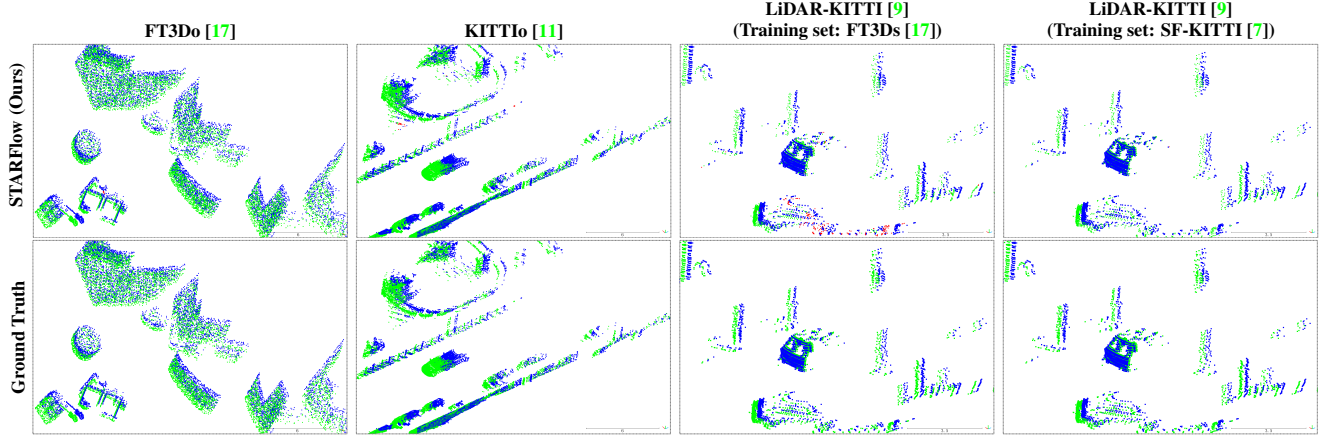


Figure 8. Qualitative comparisons between STARFlow and ground truth conducted on other datasets. Colors mean the same as Figure 7.

STR	GA	DA Loss	FT3Ds EPE3D (m)↓	KITTIo EPE3D (m)↓
✓		✓	0.0228	0.0133
	✓	✓	0.0200	0.0128
✓	✓		0.0171	0.0234
✓	✓	✓	0.0143	0.0064

Table 4. Ablation studies of distinct modules. All module combinations are trained on FT3Ds.

5.4. Ablation Study

To investigate the distinct impacts of GA, STR, and DA Losses, a set of ablation experiments are conducted to perform functional analysis. All models are trained and evaluated by employing FT3Ds and are directly tested on KITTIo. The comprehensive results of the ablation experiments can be found in Table 4, while detailed information regarding each module’s ablation is presented in Table 5 and Table 6.

GA Unlike previous methods [12, 21, 26], the GA module calculates the global query-key map between the source and target frames, obtaining match associations across all point pairs in both the 3D Euclidean space and the feature space. In (a) of Table 5, we provide a detailed list of the importance of the global query-key map, 3D Euclidean space (i.e., position encoding), and all-to-all mechanism for GA. Firstly, we exclude the global query-key map and the subsequent global attentive aggregation in GA. Then, we remove the input of 3D coordinates and solely conduct an all-to-all matching within the feature space. Ultimately, we substitute the all-to-all match method with KNN, at which point GA almost loses all its effect. After removing the global query-key map, the model experienced a substantial decline in accuracy, primarily due to its hard learnability.

STR The STR module effectively re-embeds the local spatiotemporal features of each point in the source frame after warping, resulting in a significant improvement of flow

	Method	FT3Ds EPE3D (m)↓
	Ours (full equip)	0.0143
(a)	Ours (w/o global query-key feature map)	0.0192
	Ours (w/o global query-key feature map and position encoding)	0.0203
	Ours (w/o global query-key feature map, position encoding, and all-to-all mechanism)	0.0228
(b)	Ours (w/o spatial feature re-embedding)	0.0183
	Ours (w/o temporal feature re-embedding)	0.0193

Table 5. Detailed ablations of the GA and STR modules.

\mathcal{L}_{cfs}	\mathcal{L}_{lfs}	KNN	Radius	FT3Ds EPE3D (m)↓	KITTIo EPE3D (m)↓
✓		✓	✓	0.0157	0.0089
	✓	✓	✓	0.0149	0.0080
✓	✓	✓	✓	0.0166	0.0112
✓	✓	✓	✓	0.0143	0.0064

Table 6. Detailed ablations of the DA Losses. KNN and Radius signify different neighborhood search ways.

prediction, as shown in Table 4. We remove the spatial and temporal feature re-embedding sub-modules separately to consider their contribution to the STR module. The detailed results are listed in (b) of Table 5. It is observed that the spatial feature re-embedding sub-module has brought greater performance improvement, which is in line with common sense, as the relation between the two frames has been taken into account in the subsequent cost volume calculations.

DA Losses In order to explore the details of solving the synthetic-to-real domain shift problem in scene flow tasks, we conduct a series of ablation experiments exploring the effectiveness of the local flow consistency loss and the cross-frame feature similarity loss, as well as neighborhood search strategies. The results are listed in Table 6. Detailed analysis

Model	FT3Ds EPE3D (m)↓	Param size (M)	Run time (ms)
PointPWC	0.0588	7.72	76
PointPWC+STR	0.0504	8.02	81
PointPWC+STR+GA	0.0402	9.89	96
FlowNet3D	0.1136	1.23	70
FlowNet3D+GA	0.0837	1.36	94

Table 7. Comparisons of module migration, where “+” represents module integration.

of the hyper-parameters is in the supplementary material.

Contributions to Other Models To evaluate the effectiveness of the proposed GA and STR modules, we conduct experiments by integrating them directly into PointPWC [34] and FlowNet3D [15]. Following the original training strategy as described in the respective papers, the results are listed in Table 7. Both modules improve network performance.

6. Conclusion

We propose STARFlow to accurately and robustly estimate scene flow. STARFlow conducts global attentive matching between continuous frames in both Euclidean and feature spaces. Additionally, it effectively re-embeds deformed spatiotemporal features within local refinement. The DA Losses enhance the generalization ability of STARFlow on various pattern datasets. Experiments show that our method achieves SOTA performance on multiple distinct datasets.

References

- [1] Ramy Battarawy, René Schuster, Mohammad-Ali Nikouei Mahani, and Didier Stricker. RMS-FlowNet: Efficient and robust multi-scale scene flow estimation for large-scale point clouds. In *Proceedings of International Conference on Robotics and Automation*, pages 883–889. IEEE, 2022. 2
- [2] Angel X Chang, Thomas Funkhouser, Leonidas Guibas, Pat Hanrahan, Qixing Huang, Zimo Li, Silvio Savarese, Manolis Savva, Shuran Song, Hao Su, et al. ShapeNet: An information-rich 3D model repository. *arXiv preprint arXiv:1512.03012*, 2015. 6
- [3] Wencan Cheng and Jong Hwan Ko. Bi-PointFlowNet: Bidirectional learning for point cloud based scene flow estimation. In *Proceedings of European Conference on Computer Vision*, pages 108–124. Springer, 2022. 1, 2, 4, 6, 7
- [4] Wencan Cheng and Jong Hwan Ko. Multi-scale bidirectional recurrent network with hybrid correlation for point cloud based scene flow estimation. In *Proceedings of the IEEE/CVF International Conference on Computer Vision (ICCV)*, pages 10041–10050, October 2023. 1, 2, 6, 7
- [5] Jacob Devlin, Ming-Wei Chang, Kenton Lee, and Kristina Toutanova. BERT: Pre-training of deep bidirectional transformers for language understanding. *arXiv preprint arXiv:1810.04805*, 2018. 2
- [6] Fangqiang Ding, Zhen Luo, Peijun Zhao, and Chris Xiaoxuan Lu. milliFlow: Scene flow estimation on mmwave radar point cloud for human motion sensing. *arXiv preprint arXiv:2306.17010*, 2023. 1
- [7] Lihe Ding, Shaocong Dong, Tingfa Xu, Xinli Xu, Jie Wang, and Jianan Li. FH-Net: A fast hierarchical network for scene flow estimation on real-world point clouds. In *Proceedings of European Conference on Computer Vision*, pages 213–229. Springer, 2022. 6, 7, 8
- [8] Jingyun Fu, Zhiyu Xiang, Chengyu Qiao, and Tingming Bai. PT-FlowNet: Scene flow estimation on point clouds with point transformer. *IEEE Robotics and Automation Letters*, 8(5):2566–2573, 2023. 2, 4
- [9] Andreas Geiger, Philip Lenz, and Raquel Urtasun. Are we ready for autonomous driving? the KITTI vision benchmark suite. In *Proceedings of IEEE Conference on Computer Vision and Pattern Recognition*, pages 3354–3361, 2012. 6, 8
- [10] Zan Gojcic, Or Litany, Andreas Wieser, Leonidas J Guibas, and Tolga Birdal. Weakly supervised learning of rigid 3D scene flow. In *Proceedings of the IEEE/CVF Conference on Computer Vision and Pattern Recognition*, pages 5692–5703, 2021. 6, 7
- [11] Xiuye Gu, Yijie Wang, Chongruo Wu, Yong Jae Lee, and Panqu Wang. HPLFlowNet: Hierarchical permutohedral lattice FlowNet for scene flow estimation on large-scale point clouds. In *Proceedings of the IEEE/CVF Conference on Computer Vision and Pattern Recognition*, pages 3254–3263, 2019. 6, 8
- [12] Yair Kittenplon, Yonina C Eldar, and Dan Raviv. FlowStep3D: Model unrolling for self-supervised scene flow estimation. In *Proceedings of the IEEE/CVF Conference on Computer Vision and Pattern Recognition*, pages 4114–4123, 2021. 2, 4, 8
- [13] Bing Li, Cheng Zheng, Silvio Giancola, and Bernard Ghanem. SCTN: Sparse convolution-transformer network for scene flow estimation. In *Proceedings of the AAAI Conference on Artificial Intelligence*, volume 36, pages 1254–1262, 2022. 2, 7
- [14] Hanlin Li, Guanting Dong, Yueyi Zhang, Xiaoyan Sun, and Zhiwei Xiong. RPPformer-Flow: Relative position guided point transformer for scene flow estimation. In *Proceedings of the 30th ACM International Conference on Multimedia*, pages 4867–4876, 2022. 1, 2, 7
- [15] Xingyu Liu, Charles R Qi, and Leonidas J Guibas. FlowNet3D: Learning scene flow in 3D point clouds. In *Proceedings of the IEEE/CVF Conference on Computer Vision and Pattern Recognition*, pages 529–537, 2019. 1, 2, 6, 7, 9
- [16] Ilya Loshchilov and Frank Hutter. Decoupled weight decay regularization. *arXiv preprint arXiv:1711.05101*, 2017. 6
- [17] Nikolaus Mayer, Eddy Ilg, Philip Hausser, Philipp Fischer, Daniel Cremers, Alexey Dosovitskiy, and Thomas Brox. A large dataset to train convolutional networks for disparity, optical flow, and scene flow estimation. In *Proceedings of the IEEE Conference on Computer Vision and Pattern Recognition*, pages 4040–4048, 2016. 6, 7, 8
- [18] Moritz Menze, Christian Heipke, and Andreas Geiger. Joint 3D estimation of vehicles and scene flow. *ISPRS*

- Annals of the Photogrammetry, Remote Sensing and Spatial Information Sciences, 2:427, 2015. 6
- [19] Moritz Menze, Christian Heipke, and Andreas Geiger. Object scene flow. ISPRS Journal of Photogrammetry and Remote Sensing, 140:60–76, 2018. 6, 7
- [20] Bojun Ouyang and Dan Raviv. Occlusion guided scene flow estimation on 3D point clouds. In Proceedings of the IEEE/CVF Conference on Computer Vision and Pattern Recognition, pages 2805–2814, 2021. 7
- [21] Gilles Puy, Alexandre Boulch, and Renaud Marlet. FLOT: Scene flow on point clouds guided by optimal transport. In Proceedings of European Conference on Computer Vision, pages 527–544. Springer, 2020. 1, 6, 7, 8
- [22] Yaqi Shen, Le Hui, Jin Xie, and Jian Yang. Self-supervised 3D scene flow estimation guided by superpoints. In Proceedings of the IEEE/CVF Conference on Computer Vision and Pattern Recognition, pages 5271–5280, 2023. 7
- [23] Yukang Shi and Kaisheng Ma. SAFIT: Segmentation-aware scene flow with improved transformer. In Proceedings of the International Conference on Robotics and Automation, pages 10648–10655. IEEE, 2022. 2
- [24] Deqing Sun, Xiaodong Yang, Ming-Yu Liu, and Jan Kautz. PWC-Net: CNNs for optical flow using pyramid, warping, and cost volume. In Proceedings of the IEEE Conference on Computer Vision and Pattern Recognition, pages 8934–8943, 2018. 1, 2
- [25] Ashish Vaswani, Noam Shazeer, Niki Parmar, Jakob Uszkoreit, Llion Jones, Aidan N Gomez, Łukasz Kaiser, and Illia Polosukhin. Attention is all you need. Advances in neural information processing systems, 30, 2017. 2
- [26] Guangming Wang, Yunzhe Hu, Zhe Liu, Yiyang Zhou, Masayoshi Tomizuka, Wei Zhan, and Hesheng Wang. What matters for 3D scene flow network. In Proceedings of European Conference on Computer Vision, pages 38–55. Springer, 2022. 1, 2, 4, 6, 7, 8
- [27] Guangming Wang, Yunzhe Hu, Xinrui Wu, and Hesheng Wang. Residual 3-D scene flow learning with context-aware feature extraction. IEEE Transactions on Instrumentation and Measurement, 71:1–9, 2022. 1, 2
- [28] Guangming Wang, Xinrui Wu, Zhe Liu, and Hesheng Wang. Hierarchical attention learning of scene flow in 3D point clouds. IEEE Transactions on Image Processing, 30:5168–5181, 2021. 1
- [29] Guangming Wang, Xinrui Wu, Zhe Liu, and Hesheng Wang. Hierarchical attention learning of scene flow in 3D point clouds. IEEE Transactions on Image Processing, 30:5168–5181, 2021. 2
- [30] Haiyan Wang, Jiahao Pang, Muhammad A Lodhi, Yingli Tian, and Dong Tian. FESTA: Flow estimation via spatial-temporal attention for scene point clouds. In Proceedings of the IEEE/CVF Conference on Computer Vision and Pattern Recognition, pages 14173–14182, 2021. 2
- [31] Zirui Wang, Shuda Li, Henry Howard-Jenkins, Victor Prisacariu, and Min Chen. FlowNet3D++: Geometric losses for deep scene flow estimation. In Proceedings of the IEEE/CVF winter conference on applications of computer vision, pages 91–98, 2020. 2
- [32] Yi Wei, Ziyi Wang, Yongming Rao, Jiwen Lu, and Jie Zhou. PV-RAFT: Point-voxel correlation fields for scene flow estimation of point clouds. In Proceedings of the IEEE/CVF Conference on Computer Vision and Pattern Recognition, pages 6954–6963, 2021. 4, 7
- [33] Wenxuan Wu, Zhongang Qi, and Li Fuxin. PointConv: Deep convolutional networks on 3D point clouds. In Proceedings of the IEEE/CVF Conference on Computer Vision and Pattern Recognition, pages 9621–9630, 2019. 3
- [34] Wenxuan Wu, Zhi Yuan Wang, Zhuwen Li, Wei Liu, and Li Fuxin. PointPWC-Net: Cost volume on point clouds for (self-) supervised scene flow estimation. In Proceedings of European Conference on Computer Vision, pages 88–107. Springer, 2020. 1, 2, 4, 6, 7, 9
- [35] Yanding Yang, Kun Jiang, Diange Yang, Yanqin Jiang, and Xiaowei Lu. Temporal point cloud fusion with scene flow for robust 3D object tracking. IEEE Signal Processing Letters, 29:1579–1583, 2022. 1